



# Optics Letters

## 10-million-elements-per-second printing of infrared-resonant plasmonic arrays by multiplexed laser pulses

D. PAVLOV,<sup>1,2</sup> S. GURBATOV,<sup>1,2</sup> S. I. KUDRYASHOV,<sup>2,3,4</sup> P. A. DANILOV,<sup>2,3</sup> A. P. PORFIREV,<sup>2,5,6</sup>  
S. N. KHONINA,<sup>5,6</sup> O. B. VITRIK,<sup>1,2</sup> S. A. KULINICH,<sup>1,7</sup> M. LAPINE,<sup>8</sup> AND A. A. KUCHMIZHAK<sup>1,2,\*</sup>

<sup>1</sup>School of Natural Sciences, Far Eastern Federal University, 6 Sukhanova Str., 690041 Vladivostok, Russia

<sup>2</sup>Institute for Automation and Control Processes FEB RAS, 5 Radio Str., 690041 Vladivostok, Russia

<sup>3</sup>Lebedev Physical Institute, Leninskiy prospect 53, Moscow 119991, Russia

<sup>4</sup>ITMO University, Kronverkskiy prospect 49, 197101 St. Petersburg, Russia

<sup>5</sup>Samara National Research University, Moskovskoe shosse, 34, Samara 443086, Russia

<sup>6</sup>Image Processing Systems Institute – Branch of the Federal Scientific Research Centre “Crystallography and Photonics”

of Russian Academy of Sciences, 151 Molodogvardejskaya Str., Samara 443001, Russia

<sup>7</sup>Research Institute of Science and Technology, Tokai University, Hiratsuka, Kanagawa 259-1292, Japan

<sup>8</sup>School of Mathematical and Physical Sciences, University of Technology Sydney, NSW 2007, Sydney, Australia

\*Corresponding author: alex.iacp.dvo@mail.ru

Received 25 October 2018; revised 25 November 2018; accepted 30 November 2018; posted 4 December 2018 (Doc. ID 348558);  
published 8 January 2019

We report on high-quality infrared (IR)-resonant plasmonic nanoantenna arrays fabricated on a thin gold film by tightly focused femtosecond (fs) laser pulses coming at submegahertz repetition rates at a printing rate of 10 million elements per second. To achieve this, the laser pulses were spatially multiplexed by fused silica diffractive optical elements into 51 identical submicrometer-sized laser spots arranged into a linear array at periodicity down to 1  $\mu\text{m}$ . The demonstrated high-throughput nanopatterning modality indicates fs laser maskless microablation as an emerging robust, flexible, and competitive lithographic tool for advanced fabrication of IR-range plasmonic sensors for environmental sensing, chemosensing, and biosensing. ©2019 Optical Society of America

<https://doi.org/10.1364/OL.44.000283>

Large- or lab-scale arrays of different nanophotonic elements are key building blocks of plasmonic or all-dielectric metasurfaces that enable nanoscale light control [1–4], as well as chemosensing and biosensing modalities [5–7]. A key concept underlying the metasurface functionalities is the use of constituent elements with spatially varying optical properties. Quite recently, two-dimensional pixelated all-dielectric metasurfaces exhibiting ultra-sharp discrete-frequency infrared (IR) responses were demonstrated [8], used to detect surface-bound analytes via broadband IR illumination, with nondestructive and label-free surface-enhanced IR absorption or reflection (SEIRA/R) at multiple spectral sensing points [8]. This approach paves the way toward efficient and versatile miniaturized mid-IR SEIRA sensors capable of resolving molecular fingerprints without any spectrometry tools.

Currently, both plasmonic and all-dielectric metasurfaces are commonly fabricated by optical, electron, or ion-beam lithography [7,8]. However, multiscale elements of metasurfaces, when fabricated through traditional lithographic procedures, become dramatically more expensive and require significantly longer fabrication cycles. Alternatively, near- or mid-IR-range metasurfaces can be fabricated by versatile high-performing laser-based approaches, including single-shot multi-beam laser interference lithography of moderately focused laser pulses [9,10] and shot-per-spot nanopatterning and micropatterning that use tightly focused multikilohertz laser repetition rates and fast scanning/positioning systems [11,12]. With fs-pulse lasers that provide ultimate spatial resolution via a reduced heat-affected zone [13], multibeam laser interference capability is considerably diminished by coherence length constrictions, limiting the size of single-shot fabrication areas and introducing a stitching problem. The stitching is complicated owing to non-uniform intensity distribution along the interference pattern area, resulting in further reduction in the effective processing area.

In contrast, throughput of laser nanopatterning and micropatterning can be additionally increased via beam multiplexing achieved by means of robust solid-phase diffractive optical elements (DOEs) [14–16] or cooled liquid-crystal spatial light modulators [17–20]. Scanning and multiplexing modalities provide broad flexibility during ultrashort-pulse laser nanopatterning and micropatterning for fabrication of multiscale plasmonic and all-dielectric metasurfaces. Apart from the mid-IR spectral region, where typical characteristic vibration bands of proteins and smaller organic molecules are located [7], there is also a need for high-quality surface textures resonating at near-IR excitation wavelengths, where various plasmonic-based

biosensor designs can be readily realized with a range of inexpensive telecom-band laser sources and spectrometers. However, ultra-fast galvanometric scanning systems with F-theta lenses can hardly be applicable to produce submicrometer-scale structures at micrometer periodicities.

In this Letter, we report on advanced high-throughput laser micropatterning of a gold film by highly multiplexed, tightly focused submegahertz-rate fs laser pulses, optimized to achieve submicrometer-sized structures with minimal array periodicity. We demonstrate an ultrafast (up to 10 million structural features per second) fabrication of highly ordered arrays of various nanoantennas (from nanobumps to microholes), which exhibit specific IR plasmonic responses, determined by a nanoantenna shape and arrangement.

Ultrafast surface patterning of 100-nm-thick Au films, which were e-beam deposited onto commercial silica glass slides (Kurt Lesker), was performed by second-harmonic (515 nm), 200-fs pulses of a regenerative amplified Yb:KGW-based fs laser system (Pharos, Light Conversion). The system provided very high pulse-to-pulse stability (typically 0.15%) with maximal pulse energy of 100  $\mu$ J and repetition rate of 200 KHz. The laser radiation was converted into linear arrays of 51 identical diffraction limited laser spots using specially designed DOEs [Fig. 1(a)]. Such DOEs were designed by calculating their phase-only transmission functions [typical example is given in the inset of Fig. 1(a)] using the well-known Gerchberg–Saxton algorithm [21]. The algorithm allows for reconstruction of the unknown wavefront from the known intensity distributions on a few planes of an optical system, for example in the input and the focal planes. Using a standard combination of photolithography and plasma etching, the calculated phase patterns were transferred onto fused silica substrates that provide a rather high damage threshold at a high pulse repetition rate. The resulting series of DOEs arranged within the motorized turret system for fast switching provided a linear pattern of 51 identical laser spots with a fixed  $1/e^2$  diameter of 0.78  $\mu$ m each and periodicities ranging from 1 to 1.5  $\mu$ m

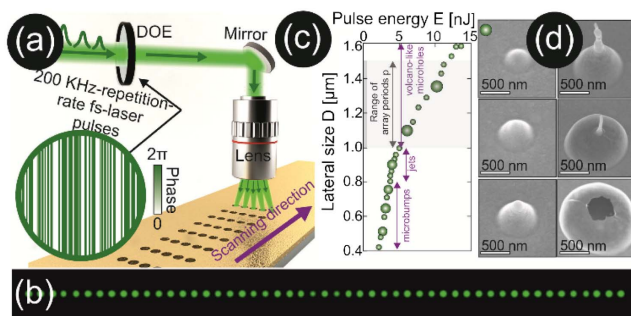


**Fig. 1.** (a) Schematic illustration of the laser fabrication approach, where 200-fs laser pulses with  $\lambda = 515$  nm coming at 200 kHz repetition rate are converted into a linear array of 51 identical diffraction-limited laser spots using specially designed DOE. The inset shows a typical DOE phase pattern providing such an intensity pattern, where each laser spot has  $1/e^2$  diameter of  $D_{1/e^2} = 0.78$   $\mu$ m each and array periodicity ( $p$ ) of 1.5  $\mu$ m. (b) Corresponding transverse intensity distribution captured in the focal plane of the microscope lens with NA = 0.42. (c) (D) Lateral size of the surface structures (nanobumps, nanojets, and volcano-like microholes) versus applied ( $E$ ) pulse energy. (d) Corresponding side-view SEM images of the laser-printed structures. These structures are shown with larger markers in (c).

[at a 515 nm laser wavelength and focusing with a lens having a numerical aperture (NA) of 0.42, Fig. 1(b)]. The transmission efficiency of all fabricated DOEs was measured to be about  $70 \pm 3\%$ , which is in good agreement with the calculated value; the fluctuation of the intensity in all the 51 laser spots within the produced linear array did not exceed 5%, which is comparable to the short-term pulse-to-pulse stability of commercially available mid-level laser systems. The moderate focusing conditions (NA = 0.42) were utilized as a tradeoff between the submicrometer spot size ( $D_{1/e^2} \sim 0.78$   $\mu$ m) and substantial focal depth, of importance considering large distances of the sample motion. Overall, the proposed optical scheme significantly simplifies fabrication of rectangular-shaped microarrays, as accurate scanning is only required along one direction, thus permitting ultrafast, straightforward, and robust fabrication.

The samples were produced using a precise nanopositioning system (Newport XMS100-S) with a traveling range of 100 mm, providing the maximal speed of  $3 \cdot 10^5$   $\mu$ m/s with high moving accuracy, which permitted use of the maximal pulse repetition rate of our laser system. Using DOE-generated linear arrays of laser spots, the printing rate of 10 million elements per second for array periodicities  $p \leq 1.5$   $\mu$ m was achieved.

First, we studied single-pulse patterning of a 100-nm-thick Au film coated onto silica glass substrate. This was done with a single laser spot having the characteristic size of  $D_{1/e^2} = 0.78$   $\mu$ m, which is equal to those of the spots in the DOE-generated pattern. This calibration procedure was required to find the appropriate pulse energy range and lateral dimensions of the surface structures that can be printed at near-threshold fluences, as well as the possibility of their denser arrangement. The lateral size ( $D$ ) of the surface structures versus ( $E$ ) the applied pulse energy is shown in Fig. 1(c), while some representative surface morphologies are illustrated by side-view scanning electron microscopy (SEM) images in Fig. 1(d). In brief, nanobumps are seen to appear first as the smallest surface modifications [left column, Fig. 1(d)], with their lateral dimensions and height gradually increasing with  $E$  [12,22]. The specific shape of such surface morphologies results from the local melting of the Au film section accompanied by its acoustic relaxation via thermal generated stresses [13]. At  $E > 4$  nJ the fs-pulse irradiation drives substantial redistribution of the molten material providing its accumulation atop a nanobump and resulting in formation of a protrusion (nanojet). Finally, at higher pulse energies ( $E > 5$  nJ), the liquid nanojets decay via ejection of droplets, until volcano-like microholes appear. Interestingly, Fig. 1(c) shows that all surface textures observed within the considered range of applied pulse energies  $E$  have submicrometer lateral dimensions  $D$  at such a beam size. This substantiates the possibility of their close arrangement, at least at the array periodicity of  $p = 1.5$   $\mu$ m. Analysis of the data from Fig. 1(c) represented in  $D^2(\ln E)$  coordinates reveals that the threshold pulse energy  $E_{th} = 2$  nJ is required to irreversibly modify a 100-nm-thick Au film, with the characteristic energy deposition diameter  $D_{1/e} \approx 1.04$   $\mu$ m. Accordingly, this provides the threshold absorbed fluence  $F_{th} = 4A \cdot E_{th} / \pi D_{1/e}^2 \approx 49$  mJ/cm<sup>2</sup>, considering a constant absorbance of  $A \approx 0.2$ , which is in agreement with an earlier study [13]. Taking into account the maximal output pulse energy of the laser source, losses in the optical system ( $\sim 30\%$ ) as well as DOE conversion efficiency, the remaining energy appears to be high enough for printing with multiplexed beams.

Using the proposed beam multiplexing technique, we produced several well-ordered square-shaped arrays, each containing  $51 \times 51$  identical elements (nanoantennas) and having periodicity  $p = 1.5 \mu\text{m}$  [Fig. 2(a)]. The shape of the nanoantennas was tuned by simply varying the applied pulse energy  $E$  in accordance with Fig. 1(c). SEM images indicate good periodicity and square-shaped arrangement of the printed arrays. Fourier-transform IR (FTIR) microspectroscopy revealed the appearance of some sharp ( $\lambda_r/\Delta\lambda_r \leq 10$ ) spectral features for the arrays containing nanobumps with the spectral position of resonance  $\lambda_r$ , shifting from 1.85 to 2.2  $\mu\text{m}$  upon increasing the structure size. When the shape of structures arranged as an array evolves from nanobumps to nanojets, the resonance becomes broader, indicating stronger deviation

of the geometric parameters of the nanoantennas within each row of the array; this was also confirmed by corresponding SEM images. The reason for this size deviation can be explained by extremely high sensitivity of the nanojet height to even very small energy fluctuations ( $\leq 5\%$ ) within each laser spot of the linear array. For nanobumps, these energy fluctuations do not cause such extremely high variations in shape, resulting in much sharper resonances. Another reason for more reproducible printing of nanobumps is related to their ablation-free formation mechanism, which involves no nanoparticle ejection and redeposition. Such nanoparticles locally reduce the ablation threshold of the as-deposited Au film via near-field EM enhancement, resulting in poorer printing quality. For the volcano-like microholes, even though their shape was reproduced much better compared to the nanojets, no evident narrow spectral features were observed in their near-IR spectra [black dashed curve, Fig. 2(a)].

To reveal the origin of the observed IR resonances, we have produced several arrays of nanobumps at applied pulse energy  $E = 2.34, 2.65,$  and  $2.9 \text{ nJ}$  and with array periodicity  $p$  from 1 to  $1.5 \mu\text{m}$  [Fig. 2(b)]. The FTIR spectra in Fig. 2(b) shows that the resonant wavelength  $\lambda_r$  depends not only on the pulse energy but also linearly scales with  $p$  [Fig. 2(c)]. This finding can be understood in terms of surface plasmon polariton (SPP) interference. Under normal irradiation, the incoming light polarized along the metal film surface can be coupled only to SPPs at the protruding laser-printed nanoantennas. The SPP waves then descend onto the film surface and interfere at mid-points between the neighboring bumps. This explanation predicts a linear scaling of the resonant wavelength  $\lambda_r$  versus the effective periodicity  $p_{\text{eff}}$  of the nanoantenna array, which is extended to include the plasmon path over the slopes of the bumps as well as the remaining section of the smooth metal film [inset in Fig. 2(d)]. By carefully measuring the relevant geometry for each nanoantenna array printed at various values of  $E$  and  $p$ , we found that the resonant wavelength  $\lambda_r$  shows the same linear dependence on the effective periodicity  $p_{\text{eff}}$  for all the experimentally measured spectra [Fig. 2(d)].

The above explanation, as well as the modulation of the resonance amplitude with the nanobump size [Figs. 2(a) and 2(b)], indicates the key role of the prepared nanoantennas in SPP coupling. More specifically, the growing size and slope of a nanobump increase coupling efficiency and effective periodicity  $p_{\text{eff}}$ . Furthermore, the spectrum measured from the nanojet array [gray-dashed curve in Fig. 2(a)] also supports the proposed model, with the effective period  $p_{\text{eff}}$  of the nanojet structure fitting nicely to the same linear trend. On the contrary, for volcano-like microholes, the broken shell does not provide efficient coupling of the incident IR radiation to the SPP waves, resulting in the absence of sharp features in the measured IR spectra. Importantly, the volcano-like microhole arrays also exhibit no resonant characteristics as one could expect from the ordinary hole arrays. Indeed, the broken shell around the microhole could be removed at higher  $E$  and larger laser spot sizes [23]. However, the increase of  $E$  was found to provide a scalable increase in the lateral size of microholes'  $D$  [see Fig. 1(c)] hindering the ability to print arrays with small periodicity, as discussed above. To overcome this problem, we take advantage of the fact that cupola walls have a thickness  $< 10 \text{ nm}$ . Thus, to produce hole arrays of good quality, we can fabricate volcano-like

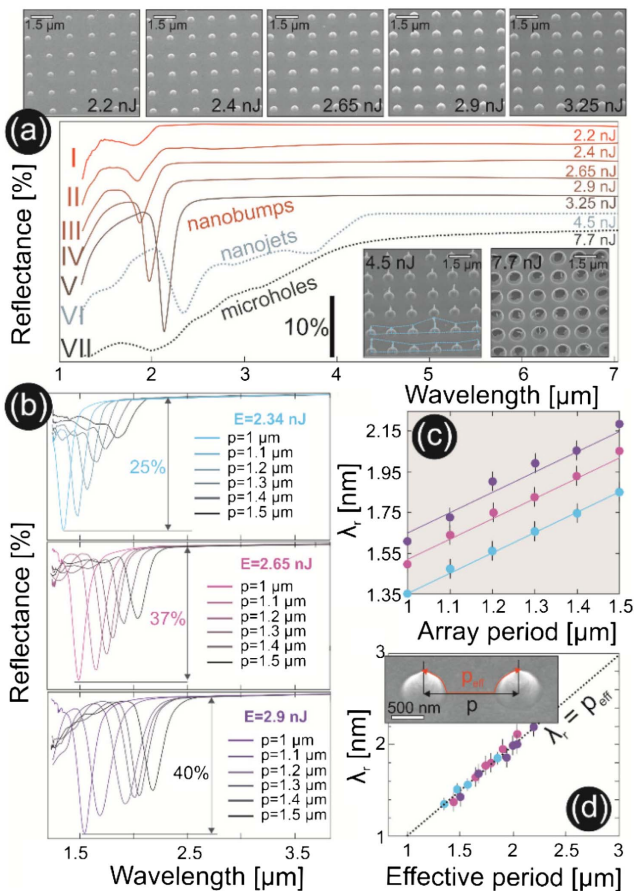


**Fig. 2.** (a) Representative side-view (view angle of  $30^\circ$ ) SEM images showing fragments of the arrays containing different types of surface nanoantennas printed at a variable pulse energy ( $E = 2.2/7.7 \text{ nJ}$  in each laser spot) using linear array of laser beams as well as normalized FTIR reflectance spectra measured from these arrays. Each square-shaped array has the identical number of structures ( $51 \times 51$ ) and the periodicity of  $p = 1.5 \mu\text{m}$ . The spectra are vertically shifted for the reader's convenience. (b) Normalized FTIR reflection spectra measured from nanobump arrays printed at three fixed pulse energies ( $E = 2.34, 2.65,$  and  $2.9 \text{ nJ}$ , from top to bottom) and variable periodicity ( $p$ ) ranging from 1 to  $1.5 \mu\text{m}$ . (c) Resonance wavelength  $\lambda_r$  versus the array period  $p$  and (d) the effective period  $p_{\text{eff}}$ .  $p_{\text{eff}}$  is determined by an actual period  $p$  and the nanoantenna circumference, as shown in the inset. The dashed line in (d) shows the linear scaling  $\lambda_r = p_{\text{eff}}$ .

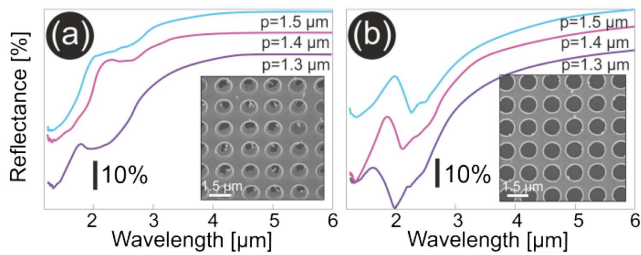


**Fig. 3.** Normalized FTIR reflectance spectra measured from array of volcano-like microholes ( $51 \times 51$  elements) (a) before and (b) after their treatment with  $\text{Ar}^+$ -ion beam for 2 min. Insets show corresponding closeup SEM images of the arrays.

microhole arrays and then process these using either chemical or ion-beam polishing to remove the broken shell.

To illustrate the possibility of such postprocessing, we produced arrays of volcano-like microholes at fixed applied pulse energy ( $E = 7.7$  nJ) and period varying from 1.3 to 1.5  $\mu\text{m}$ . Then, we treated the produced arrays with accelerated argon ( $\text{Ar}^+$ ) ions for 2 min [24], almost completely removing the thin shell and giving rise to an array of high-quality microholes (Fig. 3). The series of FTIR reflectance spectra in Figs. 3(a) and 2(b) compares the IR response of the volcano-like microhole arrays recorded (a) before and (b) after the treatment. The spectra in panel (a) have no pronounced resonant features irrespectively of the period  $p$ , whereas the spectra of the postprocessed arrays demonstrate a pronounced resonance peak with the position red shifting with an increase of  $p$ . For a perforated surface with relatively large holes, where the diameter is comparable to the structure period, plasmonic resonances are expected to be directly related to the period of the structure, being the same for reflection and transmission. As it was recently predicted [25] for such arrays, one of the factors contributing to resonances is plasmonic excitation on the outer interface, but not on the interface of incidence, so the resonance is expected when the plasmon wavelength [26]  $\lambda_{\text{SP}} = \lambda_0(1/\epsilon_1 + 1/\epsilon_2)^{0.5}$  equals the array period. On the outer interface, plasmons are running between Au film (permittivity  $\epsilon_1$  between  $-130 + 15i$  and  $-250 + 40i$  in the range from 1.8 to 2.5  $\mu\text{m}$ ) and glass substrate (permittivity  $\epsilon_2$  between 2.074 and 2.045), so we expect the resonances at  $\lambda_0$  equal to 1.89, 2.03, and 2.17  $\mu\text{m}$  for periodicity of 1.3, 1.4, and 1.5  $\mu\text{m}$ , respectively. As shown in Fig. 3, this falls within the accuracy of 5% from the measured spectra shown in panel (b). A possible explanation for this systematic discrepancy may be related to the geometry of the holes: as the latter holes were produced from jet-like formations, they might still keep some traces of the preceding cupola. That is, some parts of the Au layer could be slightly uplifted away from the substrate around the holes. As a result, this would shift the resonance wavelength toward higher magnitudes, consistent with the spectra in Fig. 3(b).

In conclusion, we have demonstrated an ultrafast (up to 10 million structural features per second) robust laser printing of plasmonic nanoantenna arrays. The produced arrays of either nanobumps or postprocessed microholes demonstrate strong plasmonic response in the near-IR spectral range, and the spectral position of the resonance can be controlled by varying nanoantenna geometry and/or array periodicity. The proposed structured arrays are quick and inexpensive to fabricate and

possess well-defined resonances, so we believe this approach is promising for the realization of various plasmonic-based devices, refractive index plasmonic sensors, and label-free, luminescence-free SEIRA molecular/gas biosensors for routine chemosensing and biosensing measurements. Similar structures can be also produced using thin films of other plasmonic materials (e.g., Ag or Cu [12,27]), as well as with multicomponent alloys, opening a route toward further functionality and application range.

**Funding.** Russian Science Foundation (RSF) (16-12-10165).

## REFERENCES

1. A. V. Kildishev, A. Boltasseva, and V. M. Shalaev, *Science* **339**, 1232009 (2013).
2. Yu. Nanfang and F. Capasso, *Nat. Mater.* **13**, 139 (2014).
3. M. Malinauskas, A. Žukauskas, S. Hasegawa, Y. Hayasaki, V. Mizeikis, R. Buividas, and S. Juodkazis, *Light: Sci. Appl.* **5**, e16133 (2016).
4. S. V. Makarov, A. S. Zalogina, M. Tajik, D. A. Zuev, M. V. Rybin, A. A. Kuchmizhak, S. Juodkazis, and Yu. S. Kivshar, *Laser Photon. Rev.* **11**, 1700108 (2017).
5. S. Walia, C. M. Shah, P. Gutruf, H. Nili, D. R. Chowdhury, W. Withayachumnankul, and S. Sriram, *Appl. Phys. Rev.* **2**, 011303 (2015).
6. P. Anders, O. Albrektsen, I. P. Radko, and S. I. Bozhevolnyi, *Sci. Rep.* **3**, 2155 (2013).
7. F. Neubrech, C. Huck, K. Weber, A. Pucci, and H. Giessen, *Chem. Rev.* **117**, 5110 (2017).
8. A. Titti, A. Leitis, M. Liu, F. Yesilkoy, D. Y. Choi, D. N. Neshev, Y. S. Kivshar, and H. Altug, *Science* **360**, 1105 (2018).
9. F. Röbler, T. Kunze, and A. F. Lasagni, *Opt. Express* **25**, 22959 (2017).
10. G. M. Burrow and T. K. Gaylord, *Micromachines* **2**, 221 (2011).
11. A. Kuchmizhak, E. Pustovalov, S. Syubaev, O. Vitrik, Y. Kulchin, A. Porfirev, S. Khonina, and S. Kudryashov, *ACS Appl. Mater. Interface* **8**, 24946 (2016).
12. X. Wang, A. Kuchmizhak, D. Storozhenko, S. Makarov, and S. Juodkazis, *ACS Appl. Mater. Interface* **10**, 1422 (2018).
13. X. W. Wang, A. A. Kuchmizhak, X. Li, S. Juodkazis, O. B. Vitrik, Yu. N. Kulchin, V. V. Zhakhovsky, P. A. Danilov, A. A. Ionin, S. I. Kudryashov, A. A. Rudenko, and N. A. Inogamov, *Phys. Rev. Appl.* **8**, 044016 (2017).
14. A. A. Kuchmizhak, A. P. Porfirev, S. A. Syubaev, P. A. Danilov, A. A. Ionin, O. B. Vitrik, Yu. N. Kulchin, S. N. Khonina, and S. I. Kudryashov, *Opt. Lett.* **42**, 2838 (2017).
15. S. Hasegawa, H. Ito, H. Toyoda, and Y. Hayasaki, *Opt. Express* **24**, 18513 (2016).
16. S. Matsuo, S. Juodkazis, and H. Misawa, *Appl. Phys. A* **80**, 683 (2005).
17. X.-W. Cao, Q.-D. Chen, L. Zhang, Zh.-N. Tian, Q.-K. Li, L. Wang, S. Juodkazis, and H.-B. Sun, *Opt. Lett.* **43**, 831 (2018).
18. R. J. Beck, J. P. Parry, W. N. MacPherson, A. Waddie, N. J. Weston, J. D. Shephard, and D. P. Hand, *Opt. Express* **18**, 17059 (2010).
19. M. Silvennoinen, J. Kaakkunen, K. Paivasaari, and P. Vahimaa, *Opt. Express* **22**, 2603 (2014).
20. B. Sun, P. S. Salter, C. Roeder, A. Jesacher, J. Strauss, J. Heberle, M. Schmidt, and M. J. Booth, *Light: Sci. Appl.* **7**, 17117 (2018).
21. R. W. Gerchberg and W. O. Saxton, *Optik* **35**, 237 (1972).
22. J. Koch, F. Korte, T. Bauer, C. Fallnich, A. Ostendorf, and B. N. Chichkov, *Appl. Phys. A* **81**, 325 (2005).
23. P. N. Danilov, S. A. Gonchukov, A. A. Ionin, R. A. Khmel'nitskii, S. I. Kudryashov, T. T. H. Nguyen, A. A. Rudenko, I. N. Saraeva, and D. A. Zayarny, *Laser Phys. Lett.* **13**, 055602 (2016).
24. S. Syubaev, A. Nepomnyashchii, E. Mitsai, E. Pustovalov, O. Vitrik, S. Kudryashov, and A. Kuchmizhak, *Appl. Phys. Lett.* **111**, 083102 (2017).
25. A. A. Zyblovskii, A. A. Pavlov, V. V. Klimov, A. A. Pukhov, A. V. Dorofeenko, A. P. Vinogradov, and A. A. Lisyanski, *JETP* **125**, 175 (2017).
26. S. Collin, *Rep. Prog. Phys.* **77**, 126402 (2014).
27. A. A. Kuchmizhak, D. V. Pavlov, O. B. Vitrik, and Y. N. Kulchin, *Appl. Surf. Sci.* **357**, 2378 (2015).